



Strength and stability in architected spine-like segmented structures

Ahmed S. Dalaq, Francois Barthelat*

Department of Mechanical Engineering, McGill University, 817 Sherbrooke Street West, Montreal, QC H3A 2K6, Canada



ARTICLE INFO

Article history:

Received 17 January 2019

Revised 24 March 2019

Accepted 4 April 2019

Available online 13 May 2019

Keywords:

Architected materials

Segmented materials

Structural stability

Topologically interlocking materials (TIMs)

ABSTRACT

Architected and segmented material designs have recently emerged as a powerful approach to increasing the strength and toughness of brittle materials. Architected materials are made of regular building blocks that can collectively slide, rotate, separate or interlock, providing a wealth of tunable mechanisms and properties. In this work we have used experiments and modeling to explore the mechanical response of idealized segmented systems made of a linear array of cubes subjected to axial pre-compression and to a transverse force. From simple tabletop experiments with playing dice with instrumented tests on 3D printed cubes and simple models, we highlight the effects of axial pre-compression, number of blocks, friction coefficient and surface morphology on strength, energy absorption (toughness) and stability (catastrophic vs. graceful failure). We identified two failure modes in this segmented system: a sliding mode where one or more blocks slide on one another, and a “hinging” mode where some interfaces open and rotate about hinge points. The failure mode transition between hinging and sliding was established, to assist the design of modern architected structures and materials. Finally, we demonstrate that enriching the morphology of the cubes with curved interfaces (akin to the vertebrae in the spine of reptiles) delays hinging and improves stability.

© 2019 Published by Elsevier Ltd.

1. Introduction

Specific microstructures, heterogeneities or hybrid compositions are now widely used in modern materials to generate high performance (Ashby, 2005). These concepts are now pushed to the extreme with architected materials, which contain highly controlled structures and morphological features at length scales intermediate between the microscale and the size of the component. Architected materials include composites (Ashby, 2005; Dalaq et al., 2016) and the now well-studied lattice materials (Abueidda et al., 2016; Ashby, 2006; Ashby et al., 2000; Gibson et al., 1982), which contain only a small fraction of solid. In contrast, the much less studied dense architected materials are fully solid and are made of building blocks of well-defined size and shape, arranged in two or three dimensions (Barthelat, 2015; Mirkhalaf et al., 2016, 2018b; Siegmund et al., 2016). The building blocks are stiff so their deformation remains small and within elastic limits, but the interfaces between the blocks can channel cracks and generate nonlinear deformations by frictional sliding. Building blocks can therefore collectively slide, rotate, separate or interlock, providing a wealth of tunable mechanisms and properties (Barthelat, 2015). These information-rich materials can be designed with specific architectures, geometries and interfaces to generate unusual and attractive

combinations of properties and functionalities. For example architecture can be used to combine high strength and toughness (two properties which are mutually exclusive in traditional engineering materials (Dyskin et al., 2001; Ritchie, 2011), Fig. 1a, b), or enhance impact resistance (Mirkhalaf et al., 2016) and ballistic performance (Wadley et al., 2013) in glasses or ceramics. Mechanical response is largely governed by the interactions between the blocks, which can be captured using load line analysis (Khandelwal et al., 2012), finite elements (Dugué et al., 2013; Khandelwal et al., 2012), or discrete element methods (Dugué et al., 2013; Zhu et al., 2008). Some of these concepts and mechanisms were inspired from masonry, where the fabrication of large structures was made possible by block by block assembly. Stiff building blocks with weaker interfaces also lead to crack deflection and to the containment of damage in large structures (Barthelat, 2015; Barthelat et al., 2016b; Dyskin et al., 2001; Ming-Yuan and Hutchinson, 1989; Mirkhalaf et al., 2014). Interestingly, nature has been making use of architected materials for millions of years. In bone, teeth or mollusk shells, the interplay between the shape, size, properties and arrangement of the building blocks generates, together with nonlinear behavior (resulting from viscoplastic, friction and contact based deformations) at the interfaces, powerful combinations of stiffness, strength and toughness (Barthelat, 2015; Barthelat et al., 2016b; Wegst et al., 2015). At larger length scales the segmentation of stiff elements which can move with respect to one another generates unusual combination of properties in hard surfaces with

* Corresponding author.

E-mail address: francois.barthelat@mcgill.ca (F. Barthelat).

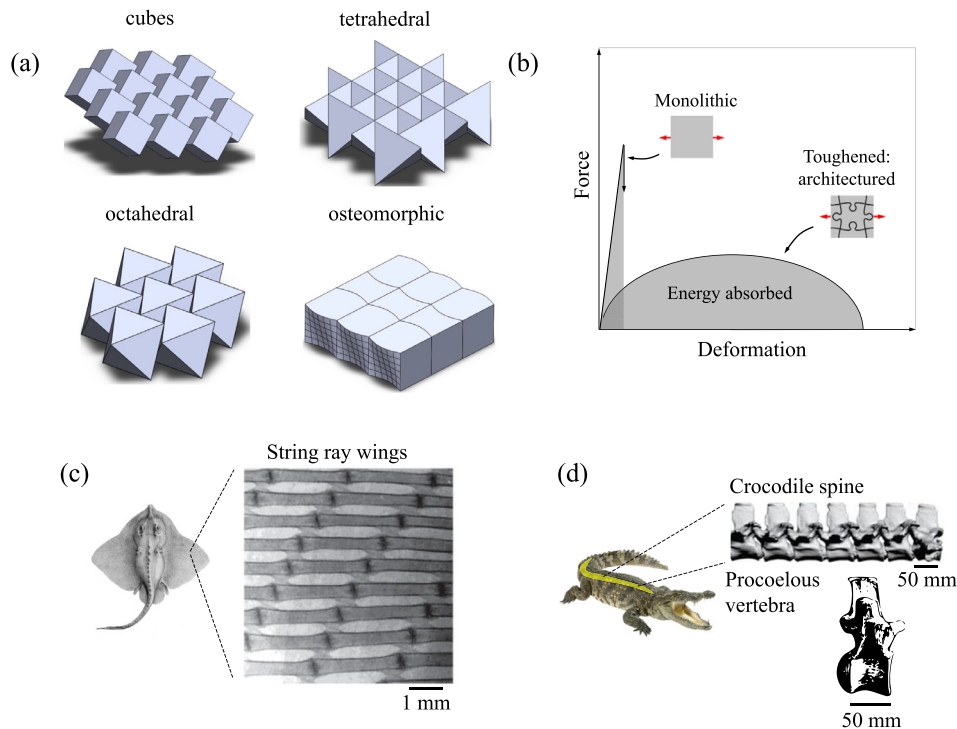


Fig. 1. Examples of synthetic and natural architected materials: (a) topologically interlocked materials (TIMs); (b) typical force-displacement response of architected materials versus monolithic materials. Linearly segmented architected materials in nature: (c) wings of a stingray fish: *Pteromylaeus asperrimus* (adapted from (Schaefer and Summers, 2005)) and (d) concavo-convex vertebrae in the crocodile spine (adapted from (Molnar et al., 2015)).

prismatic architectures to resist wear in teeth (Escobar de Obaldia et al., 2016) or segmented armor in scales and osteoderms for flexible protection (Chintapalli et al., 2014; Martini et al., 2017; Martini and Barthelat, 2016; Szewciw et al., 2017; Yang et al., 2013). The spines of vertebrae is in essence a linear arrangement of stiff elements with controlled shape (Dunn et al., 2006; Oxland, 2016), size and interfaces that allows controlled flexural deformations. For example the vertebral column of dogfish sharks can behave like a spring or a brake depending on tailbeat frequency (or bending frequency) (Porter et al., 2016). Fins and shark vertebrae are linear arrays of bony segmented mineralized blocks arranged linearly and connected by a collagenous membrane (Fig. 1c) (Alben et al., 2007; Porter et al., 2016; Schaefer and Summers, 2005). The morphology of the interfaces between vertebrae plays an important role in the overall mechanics of the spine. Some reptiles have concave and/or convex round interface articulation between their vertebrae (Fronimos et al., 2016; Troxell, 1925). These ball-and-socket like interfaces are prominent in animals that require a high range of motion with a combination of strength, toughness, and flexibility such as crocodiles, dinosaurs and lizards (Fig. 1d) (Molnar et al., 2015; Robert, 1960; Troxell, 1925). The depth of concave-convex joints varies along the spine, and is generally deeper in the neck because it is the most flexible section of the spine. To date, only a few biomimetic materials have successfully incorporated these concepts (Chen et al., 2007; Dimas et al., 2013; Mirkhalaf et al., 2014). Despite recent efforts in unifying designs (Barthelat et al., 2016a; Fratzi et al., 2016; Naleway et al., 2015) and optimization (Barthelat, 2014; Begley et al., 2012), there are still no comprehensive guidelines to select optimum architectures for given applications and requirements. This report presents a systematic mechanical analysis of linear segmented systems. We examine the strength and stability of a row of cubic idealized stiff elements under axial confinement and subjected to transverse loading. We established deformation and failure maps as function of friction coefficient

and number of cubes, and we assess the effect of simple geometric enrichment on the mechanics and stability of this type of systems.

2. “Tabletop” experiments with dice

Some of the basic deformation mechanisms and mechanical stability of linear assemblies of blocks can be captured with arrays of dice. Two playing dice can be easily lifted from a table by pressing them together (Fig. 2). It is also relatively easy to pick up a row of three, four and up to about six dice in the same manner, provided that the axial force exerted by the fingers is high enough to prevent the dice from slipping on one another. In these examples fingers confine the blocks together and act as and “external ligament”, akin to rigid frames in TIMs (Mirkhalaf et al., 2018a,b; Siegmund et al., 2016) or ligaments in spine (Oxland, 2016). Picking up longer rows of dice up to nine dice is possible, but requires special care to align the dice and to distribute the axial pressure evenly. Using two hands to apply end pressures, rows of up to 12–13 dices can be lifted from a flat surface, but the row is very unstable even with perfect alignment of the dice. The stability of a row of dice, once it has been picked up, may be assessed by applying a transverse force half-way along its length (Fig. 2). The amount of force required to collapse the row of dice may then be used as a measure of stability. By this measure, rows with $N=2$ are very stable. In rows of $N=3, 4$ or 5 dice, the center dice (or couple of dice if N is even) slide on one another to about 1/3 of their width, after which the system fails catastrophically. When a transverse force is applied on rows with $N > 6$, no sliding occurs and instead, dices near the center of the row separate and form a hinge. The two sections of the row rotate until a critical displacement is reached, leading to catastrophic collapse. All experiments suggest that long rows of dice (large N) are much less stable than shorter rows. For example, for $N=10$ the critical transverse force is very small, even when a large axial force is applied. These seemingly sim-

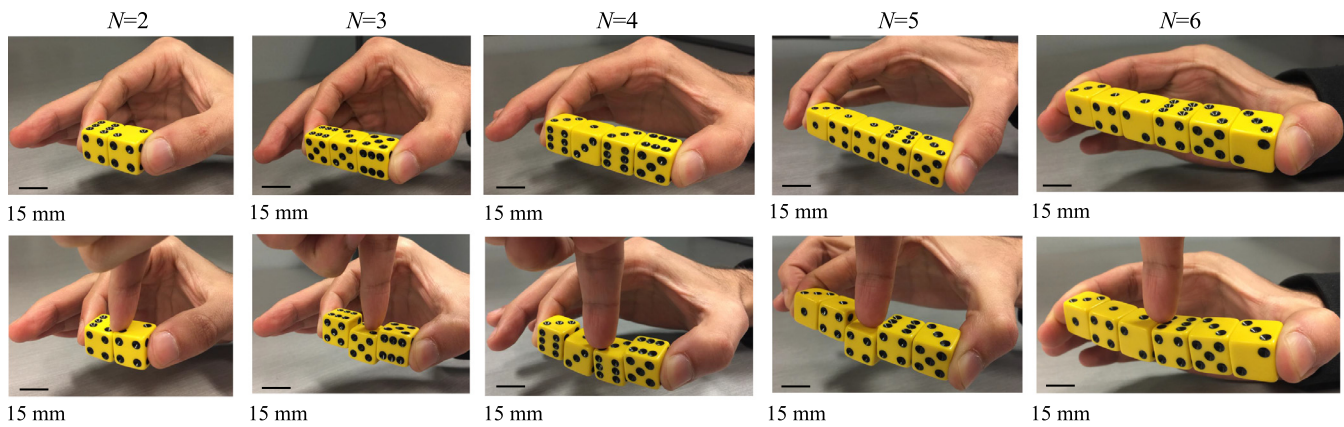


Fig. 2. Simple experiments with rows of dice ($N=2-6$). An axial pre-compression is applied with thumb and index fingers. The failure mode and the stability of the system can be assessed by applying a transverse force half-way along the dice row.

ple systems and experiments indicate that the stability, transverse strength of a row of cubes are governed by load transfer and interface mechanisms which are not trivial.

3. Instrumented experiments

We developed better controlled experiments with instrumentation that duplicated the “dice” experiments discussed above (Fig. 3a). Individual cubes ($L^3 = 5 \text{ mm} \times 5 \text{ mm} \times 5 \text{ mm}$) were 3D printed using the Digital Light Processing (DLP) technology (Micro HiRes Machine, EnvisionTech, 2019) with an ABS UV-curable polymer (3DM-X Green). We used 3D printing to fabricate the cubes because with this method the geometry of the blocks can easily be enriched (as discussed in the last section of this article). The DLP printing method also enables high spatial resolution ($\sim 80 \mu\text{m}$), a critical requirement for reproducibility, smooth surfaces and high morphological control (Dawood et al., 2015). In addition, DLP produces materials that are pore-free, homogenous and isotropic (Stuart, 2016; Tumbleston et al., 2015) ensuring uniform and consistent elastic and frictional properties. The elastic modulus of the fully cured material is $E = 1.48 \pm 0.05 \text{ GPa}$ (measured using a standard tensile test).

We measured the friction coefficient between the ABS cubes using a standardized method (ASTM D1894) (ASTM, 1894). The sliding force displayed the typical characteristics of friction, with an initial peak to initiate sliding from the static case (providing a “static” friction coefficient f_s), and a sliding force fluctuating around an average value which provides a “dynamic” friction coefficient f_d). For dry interfaces we measured coefficients of friction $f_s = 0.18 \pm 0.02$ and $f_d = 0.12 \pm 0.02$. There was some fluctuations in force in the sliding regime corresponded to slick-slip, a common phenomenon for dry polymeric surfaces (Berman et al.,

1996; Menezes et al., 2013). We explored the effects of lower friction at the interfaces between the cubes by lubrication with white sulfonated grease. These interfaces showed no stick-slip, with a lower coefficient of friction equal to $f_s = f_d = 0.11 \pm 0.01$. On the other hand, we also explored the effects of increasing friction coefficient, by treating the surfaces with an anti-slip spray (Rust-Oleum speckle spray) which produced coefficients of friction $f_s = f_d = 0.23 \pm 0.03$. For the stability experiments, 3D printed cubes were arranged and aligned into a segmented beam of N cubes. The beam was mounted on a vise used to apply an axial compressive force F_A at the ends of the row (Fig. 3b). F_A was measured with a low-profile force sensor (FlexiForce®, Tekscan). We used different values for F_A ($F_A = 10$ to 200 N), making sure that these axial forces were well below the force to plastically deform individual cubes ($F_Y \approx 1600 \text{ N}$). The compressed segmented beam was then placed in a dual column loading stage (Admet, model eXpert 5000, MA US), and a round nozzle ($R = 1.5 \text{ mm}$) fixed to the crosshead was used to impose a displacement u in the direction transverse to the beam, at a rate of $10 \mu\text{m}/\text{sec}$. The transverse force F_T was measured using a 150 lbf load cell. Fig. 4 shows a set of representative force-displacement curves $F_T - u$ obtained from beams made of $N=3$ to $N=10$ cubes. In all cases the transverse force F_T initially increased linearly with displacement. In that linear regime, the segmented beam behaved like a homogenous, continuous elastic beam, and as a result the initial stiffness was lower for higher N (i.e. longer beams). When the number of cube was small ($N < 7$), the linear region ended with a series of sudden drops at a critical sliding force $F_T^{(s)}$ and at a displacement of about $u^{(s)} \approx 0.3 \text{ mm}$ (the superscript $^{(s)}$ denotes the onset of sliding). The stiff vise maintained constant axial displacement during experiments. The contact area between the cubes decreased linearly with sliding distance, resulting in a linear decrease of F_A and therefore in the

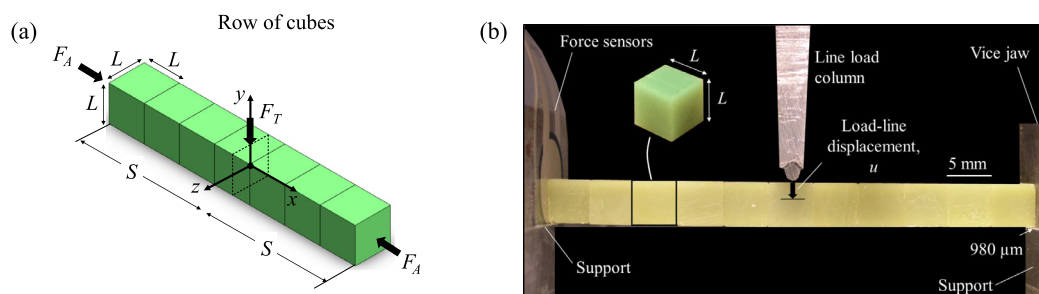


Fig. 3. A segmented beam model and the experimental setup: (a) a row of cubes with sides of $L \times L \times L$, compressed from both ends with a force F_A and loaded halfway along the span S with a transverse force F_T ; (b) 3D printed cubes made from ABS polymer ($L = 5 \text{ mm}$) arranged linearly and pre-compressed axially. A loading machine is then used to impose a transverse displacement half-way along the system and to record the corresponding force.

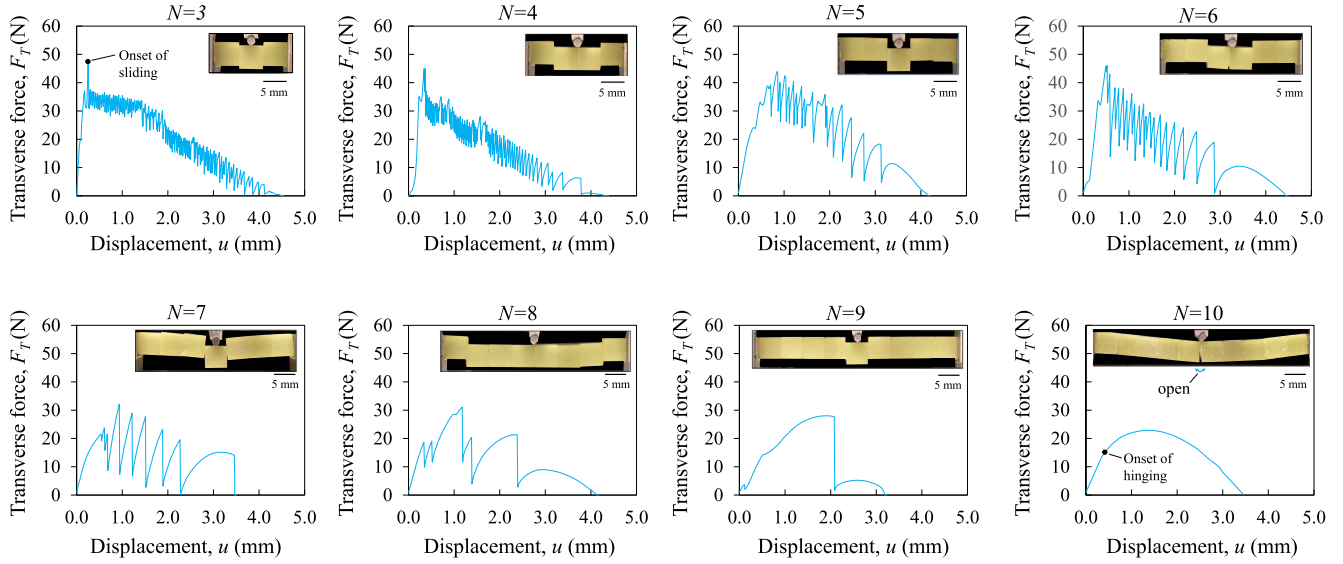


Fig. 4. Experimental force-displacement $F_T - u$ curve for the segmented cubes with different number of cubes ($N=3$ through 10), for $f_s = 0.18 \pm 0.02$, $f_d = 0.12 \pm 0.02$ and with axial pre-compression $F_A = 150$ N. The failure mode transitions from sliding to hinging as N is increased.

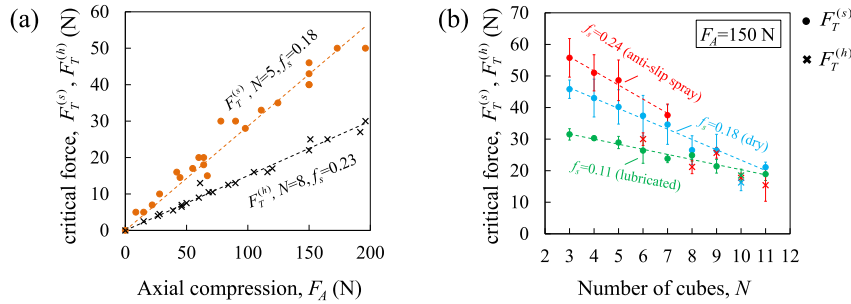


Fig. 5. Critical sliding force $F_T^{(s)}$ and hinging force $F_T^{(h)}$ as function of (a) axial pre-compression F_A and (b) number of cubes N .

observed linear decrease of F_T with sliding distance. F_T vanished at $u \approx 4$ mm, at which point the beam collapsed. Throughout the sliding of cubes, large fluctuations of forces were associated with stick slip, a typical phenomenon for materials where the dynamic friction coefficient f_d is lower than the static friction coefficient f_s (Berman et al., 1996; Menezes et al., 2013). The amplitude of the stick-slip force fluctuations was larger for higher N , because the larger volume of elastically deformed material stored more strain energy between each slip pulse.

The segmented beams with $N=7$ to 10 cubes produced a very different type of response. The $F_T - u$ curve showed a nonlinear region before the cubes started to slide (if any sliding took place at all), which corresponded to the progressive opening and loss of contact of the interfaces, together with the relative rotations of individual cubes. In the case $N=7$ and $N=8$ sliding was still observed, but with much less stick-slip. For $N=9$, only one long slip was recorded for each experiment and for $N=10$ no sliding was observed. In that case the $F_T - u$ curve had a parabolic shape, and the only failure mode being the opening of the central interface, the formation of a hinge underneath the loading pin and of two additional hinge points at the ends of the beam. In the softening region of the curve, the two segments of beam rotated about these hinge points. With the case $N=10$ we confirmed that the point at which the $F_T - u$ curve deviated from a linear response matched the onset of hinging (Fig. 4, $N=10$), occurring at the critical hinging force $F_T^{(h)}$ where the superscript (h) denotes the onset of hinging.

We found that the critical sliding force and the hinging force are both proportional to the axial pre-compression F_A . Fig. 5a

shows an example of these results for a sliding case ($N=5$ with $f_s=0.18$ on Fig. 5a) and for a hinging case ($N=8$ with $f_s=0.23$ on Fig. 5a). The experiments also confirmed that the critical force at sliding $F_T^{(s)}$ decreases linearly with increasing N , and also that the critical force decreases when f_s is decreased (Fig. 5b). Cases were hinging dominated, plotted as crosses on Fig. 5b, occurred at the highest friction coefficient. The critical force for hinging also decreases with N and is independent of f_s (Fig. 5b). From these experiments we captured the trends and the effect of f_s , of both critical forces at sliding and hinging. These experiments guided the assumptions to be made for predicting $F_T^{(s)}$ and $F_T^{(h)}$ in Section 4 and 5. The prominent failure mode is found by comparing the predicted onsets of sliding $F_T^{(s)}$ and hinging $F_T^{(h)}$. If $F_T^{(s)} < F_T^{(h)}$, sliding prevails and if $F_T^{(s)} > F_T^{(h)}$, hinging prevails.

4. Modeling the onset of sliding

An analysis based on Coulomb’s frictional force (stable friction dynamics) predicts that sliding starts when the shear force between the blocks reaches $f_s F_A$ (2013). This simple approach predicts that any of the cubes is a candidate for sliding, and that the critical transverse force for sliding does not depend on the number of cubes. The experimental observations contradict both predictions. In the experiments, only certain cubes on the beam actually slide (near the loading nose and near the supports), and the critical transverse force decreases when N is increased (Fig. 5b). Capturing the mechanics of sliding in the segmented beam therefore requires a more detailed analysis. We consider a segmented beam of length $S=NL$ made of N cubes of size $L \times L \times L$ (Fig. 6). The

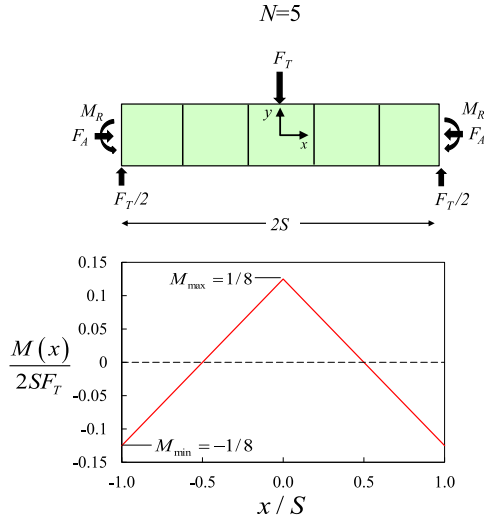


Fig. 6. Load analysis for a row of 5 cubes showing the distribution of bending moment.

material of the cubes is modeled as homogenous and isotropic, and it is assumed to follow linear elasticity with an elastic modulus E and Poisson's ratio ν . An axial compressive force F_A is applied along the x -axis, and a transverse force F_T is exerted exactly half-way along the beam and along the y -axis. The effect of gravity is neglected because the magnitudes of the applied forces are significantly higher than the gravitational body forces. The ends of the beam are assumed to be clamped, giving rise to a pair of reaction forces R and reaction couples M_R acting at both ends (Fig. 6). The system is symmetric in terms of geometry and loading about the center of the beam. The moments along the beam are written (Appendix section A.1):

$$\frac{M(x)}{2SF_T} = \frac{1}{8} \left(1 - 2 \frac{|x|}{S} \right) \quad \text{for} \quad -1 \leq \frac{x}{S} \leq 1 \quad (1)$$

The bending moment along the x -direction is minimum at the two ends: $M_{\min}/2F_T S = -1/8$ at $x/S = -1.0$ and $x/S = 1.0$ and is maximum $M_{\max}/2F_T S = 1/8$ at the center $x/S = 0$ (Fig. 6).

The bending moment $M(x)$ and the (compressive) axial force F_A both give rise to an axial stress σ_{xx} which can be obtained by superposition, since the system is linear before the cubes start sliding (Appendix section A.2):

$$\frac{L^2 \sigma_{xx}}{F_A} = 3 \frac{y}{L} \frac{F_T}{F_A} \frac{2S}{L} \left(-\frac{1}{2} + \frac{|x|}{S} \right) - 1 \quad \text{for} \quad -1 \leq \frac{x}{S} \leq 1 \quad (2)$$

$$\frac{L^2 \tau_{xy}}{F_A} = \pm 3 \frac{F_T}{F_A} \left[\left(\frac{y}{L} \right)^2 - \frac{1}{4} \right] \quad \text{for} \quad \frac{x}{S} < 0 \text{ and } \frac{x}{S} > 0 \quad (3)$$

where $2S/L$ is the number of cubes N . A microslip occur when the shear stress at a point along an interface reaches or exceeds the local "frictional" strength: $\tau_{xy} \geq f_s \sigma_{xx}$ (Ben-David et al., 2010; Ben-David and Fineberg, 2011; Johnson, 1987; Rubinstein et al., 2004). Therefore, the criterion for microslip is based on the ratio:

$$\frac{1}{f_s} \left| \frac{\tau_{xy}}{\sigma_{xx}} \right| = \frac{1}{f_s} \frac{3 \left[\left(\frac{y}{L} \right)^2 - \frac{1}{4} \right]}{3 \frac{y}{L} \frac{2S}{L} \left(-\frac{1}{2} + \frac{|x|}{S} \right) - \frac{F_A}{F_T}} \quad \text{provided} \quad \frac{x}{S} \neq 0 \quad (4)$$

Fig. 7 shows a contour plot of $|\tau_{xy} \geq f_s \sigma_{xx}|_{\max}$ at the onset of microslip, $|\tau_{xy} \geq f_s \sigma_{xx}|_{\max} = 1$ when $F_T/F_A = 0.223$ for $N=5$ and $F_T/F_A = 0.212$ for $N=8$. Fig. 7 also shows the tendency of sliding in each interface by showing the ratio $|\tau_{xy} \geq f_s \sigma_{xx}|_{\max}$ for odd case ($N=5$) and even case ($N=8$). This plot compares the tendency of sliding at each interface, where interfaces that satisfy $|\tau_{xy} \geq$

$f_s \sigma_{xx}|_{\max} = 1$ first are the "critical interfaces" that will slide and govern the failure mode of the segmented beam. Because of symmetry about the center ($x=0$), these critical interfaces come in pairs and are located at $x/L = -0.5, 0.5$ (odd) and $x/L = -3, -1, 1, 3$ (even) which can be generalized as $x/L = -0.5, 0.5$ (first row of Fig. 7a) and $x/L = 1 - N/2, -1, 1, 1 + N/2$ (first row of Fig. 7b) for odd and even cases, respectively. Critical interfaces for even cases have the same $|\tau_{xy} \geq f_s \sigma_{xx}|_{\max}$ ratio because they are subjected to the same shear forces and moments (Fig. 6). The last row in Fig. 7 shows the snapshots taken during experiments for odd and even cases that sled. Sliding interfaces in the experimental snapshots match the predicted critical interfaces (i.e. the one with the highest $|\tau_{xy} \geq f_s \sigma_{xx}|_{\max}$). These "critical interfaces" predictions are not limited to the two cases shown on Fig. 7, we compared these predictions to up to 15 cubes cases, the predictions are also in agreement with the snapshots shown on Fig. 4.

A general interface having $f_d < f_s$ will experience multiple microslips (and stick-slip). If f_d is low enough to allow for a large microslip distance, the sliding is catastrophic and the onset of microslip cascades into the sliding of the entire interface (Ben-David et al., 2010; Ben-David and Fineberg, 2011; Kammer et al., 2015; Rubinstein et al., 2004; Scheibert and Dysthe, 2010). For dry friction it is common to have $f_d < f_s$ and therefore we expect the stick slip behavior seen earlier (Fig. 4). Since sliding interfaces matched that of the catastrophic onset of sliding and $f_d < f_s$ we considered the onset of the first microslip as the onset of sliding, $|\tau_{xy} \geq f_s \sigma_{xx}|_{\max} = 1$.

Now using the onset of sliding condition: $|\tau_{xy} \geq f_s \sigma_{xx}|_{\max} = 1$ and solving for the transverse force F_T we get the critical sliding force $F_T^{(s)}$ for both odd and even cases as follows,

$$\frac{F_T^{(s)}}{F_A} = \frac{16f_s}{3(4 + f_s^2(N-2)^2)} \quad \text{at} \quad \frac{x}{L} = 0.5 \quad \text{for (odd case)} \quad (5)$$

$$\frac{F_T^{(s)}}{F_A} = \frac{16f_s}{3(4 + f_s^2(N-4)^2)} \quad \text{at} \quad \frac{x}{L} = 1 \quad \text{for (even case)} \quad (6)$$

The analytical model predicts that the critical force $F_T^{(s)}$ is proportional to the axial force F_A , which is consistent with the experiments (Fig. 5a). Fig. 8a compares the predicted critical sliding force $F_T^{(s)}$ with the experimental results. The analytical model properly captures the decrease in $F_T^{(s)}$ with increasing N (Fig. 8a), and the predicted trends follow the experimental results closely. However the experimental results are about 18% higher than the prediction, because the experimental critical force for sliding may be the results of several microslips (while the analytical result only predict the onset of the first microslip) (Ben-David et al., 2010; Rubinstein et al., 2004; Scheibert and Dysthe, 2010). The analytical model can be extended to capture the full force-displacement $F_T - u$ curve for the segmented beam. The $F_T - u$ curve before the onset of sliding corresponds to the elastic deformation of the beam and it is given by (Appendix section A.3):

$$F_T = \frac{16EL}{N^3} u \quad \text{for} \quad 0 \leq u \leq u^{(s)} \quad (7)$$

where $u^{(s)}$ is the displacement at the onset of sliding. The force after the onset of sliding is governed by friction, and can be written (Appendix section A.4):

$$\frac{F_T}{F_A} = f_d \left(1 - \frac{u}{L} \right) \quad \text{for} \quad u^{(s)} \leq u \leq L \quad (8)$$

Fig. 8b compares this model with experimental $F_T - u$ curves for $N=5$. The analytical model prediction is in good agreement with the experimental results. Discrepancies in initial modulus were attributed to non-perfect contact between the cube and to "interface compliance", as well the end conditions in the experiments which may be more compliant than the perfectly clamped

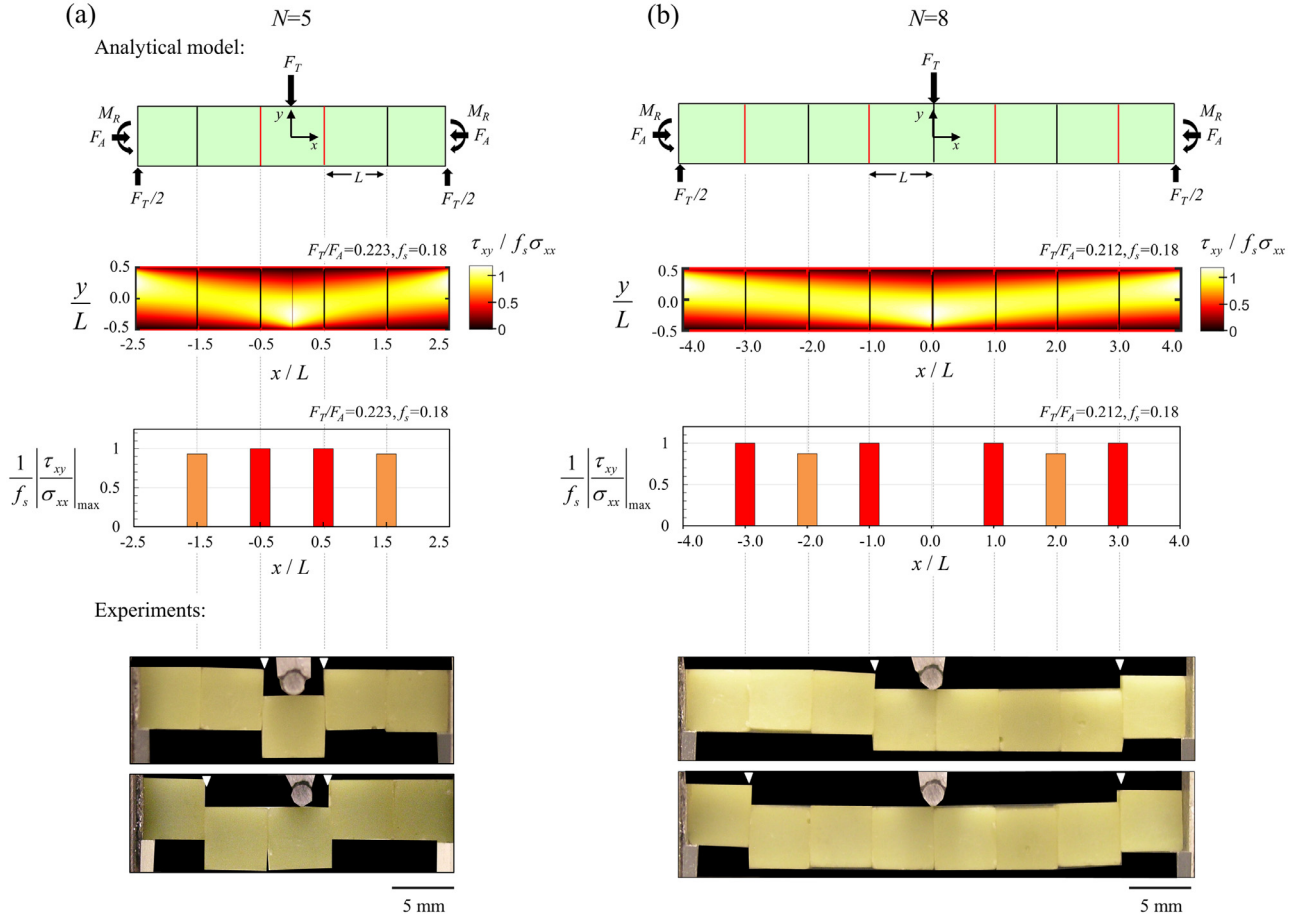


Fig. 7. Maps of sliding ratio: $|\tau_{xy}| \geq f_s \sigma_{xx, \max}$, locations of the critical interfaces and experimental snapshots of the sliding cubes for (a) an odd case ($N=5$) and (b) an even case ($N=8$).

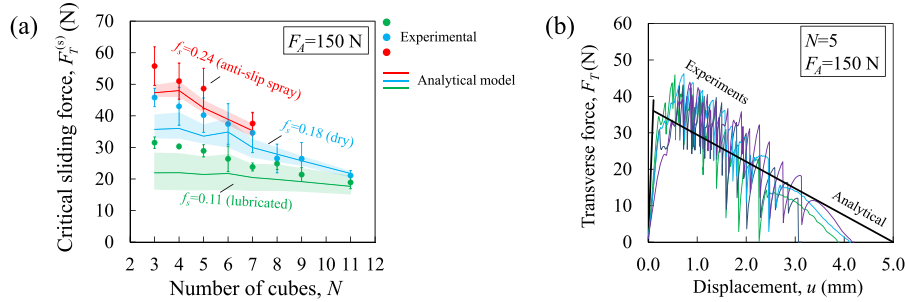


Fig. 8. Comparisons of model predictions with experiments: (a) critical sliding force as function of the number of cubes and friction coefficient; (b) force-displacement ($F_T - u$) curves.

conditions assumed in the model. The area under $F_T - u$ can be written as $U/LF_A \approx f_d$ where U represents and estimates the energy dissipated during sliding which also represents the toughness of the segmented beam.

5. Modeling the onset of hinging

In the configurations with large N , the experiments showed that the interfaces between the cubes may lose contact and form hinge points. This type of failure mode, shown for $N=10$ in Fig. 4, occurs when the initial compressive stress from the axial force F_A is completely offset by tensile stresses from the bending moment. Since the interfaces cannot carry tensile stresses they will open and form

hinges at certain points in the system where:

$$\frac{\sigma_{xx}}{F_A/L^2} = 0 \tag{9}$$

Recalling Eq. (2), this criterion can be written:

$$1 + \frac{L^2 \sigma_{xx}}{F_A} = 3 \frac{y F_T}{L F_A} \frac{2S}{L} \left(-\frac{1}{2} + \frac{|x|}{S} \right) \tag{10}$$

This criterion is illustrated in Fig. 9 as a contour plot at the onset of hinging when $F_T/F_A=0.19$ for $N=9$ and $F_T/F_A=0.16$ for $N=8$. We monitor the criterion $1 + \frac{\sigma_{xx}}{F_A/L^2}$ where value of 1 means that the interface opens at that point (to be consistent with the sliding criterion presented above). The contour plot shows region of higher

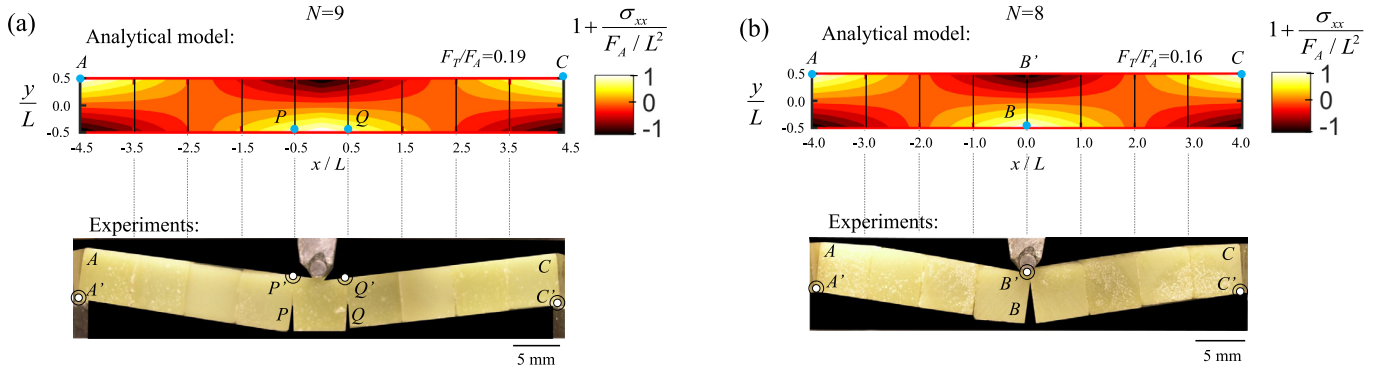


Fig. 9. Distribution of the interface opening criterion: $1 + \sigma_{xx} L^2 / F_A$ across the whole beam for (a) odd and (b) even cases. Snapshots of the experiment during hinging is shown below the contour plots to compare it with analytical predictions for the hinging points.

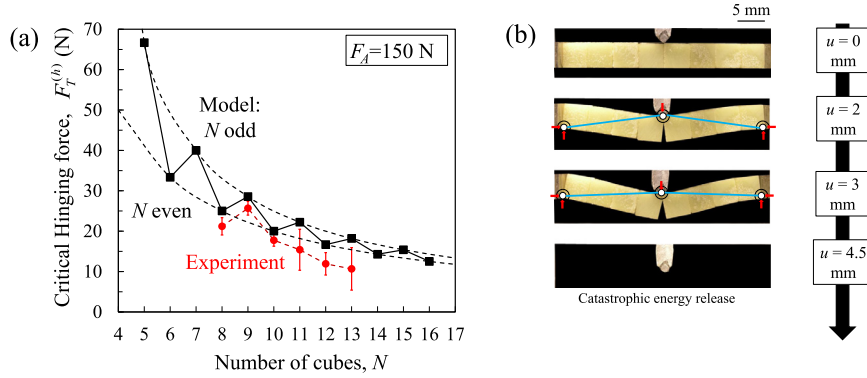


Fig. 10. (a) Critical hinging force $F_T^{(h)}$ as function of number of cubes, model prediction and experiments; (b) snapshots of the hinging process, with the load lines highlighted.

tensile stress near the upper ends of the beam, and in the lower side of the center regions.

The regions of highest stresses in this contour map can be matched with the positions of the interfaces to predict which interfaces will open first. For example for the case shown in Fig. 9a (odd number of cubes), the points that are going to open are A, P, Q and C, forming hinges at point A', P', Q' and C'. For the case shown in Fig. 9b (even number of cubes), the points that are going to open are A, B and C, forming hinges at point A', B' and C'. Snapshots from our experiments confirm these predictions. Solving for the force that satisfies the opening criterion at these points we find the critical force $F_T^{(h)}$ that causes these points to open:

$$\frac{F_T^{(h)}}{F_A} = \frac{4}{3N} \quad \text{for (even case : point A, B and C open)} \quad (11)$$

$$\frac{F_T^{(h)}}{F_A} = \frac{4}{3(N-2)} \quad \text{for (odd case : point A, P, Q and C open)} \quad (12)$$

Fig. 10a shows the experimental and analytical critical force at hinging $F_T^{(h)}$ as function of the number of cubes. $F_T^{(h)}$ decreases rapidly when N increases because the bending stresses increase with N . $F_T^{(h)}$ is lower for even cases and therefore it is easier to hinge an even number of cubes case than an odd case. For even cases, $F_T^{(h)}$ is lower because the critical points are subjected to higher moments than that of the odd case (Fig. 6). The analytical model captures the decreasing trend quite well but consistently predicts higher $F_T^{(h)}$ in comparison to the experimental measurements, reaching up to 16% error. This deviation can be attributed to non-perfect contact between the cubes where the interfaces can be more compliant than the bulk material. In addition, the end condition in the experiment may be more compliant than the model

where perfectly clamped conditions are assumed. The apparent elastic modulus at the interfaces can be slightly lower due to local point contact at the hinging points (e.g. P', Q' or B' on Fig. 9) in the case of hinging.

The mechanical response that follows the onset of hinging may be captured with a thrust line analysis (Dugué et al., 2013; Khan-delwal et al., 2012; Siegmund et al., 2016). The rotating section of the beams are confined axially and therefore develop compressive stresses from the geometric jamming. These compressive stresses are channeled in each section of beam through two hinge points which only transmit forces, and therefore each section can be considered as a two dimensional two-force member (or thrust member) for the purpose of the analysis (Fig. 10b). While this idealization is simple, the detailed force-deflection curve can be difficult to obtain because of geometric nonlinearities in the system (large rotations and non-linear contact stiffness at the hinges). Nevertheless, the thrust line analysis can provide two useful insights: first, unlike sliding failure mode that dissipates energy, the hinging deformation mode only involves elastic deformation and therefore it does not dissipate energy. Second, the hinging deformation mode is stable as long as the compressed thrust line can carry the applied force. When these lines become horizontal they cannot balance the applied force and the system becomes unstable (Fig. 10b). This threshold marks the point of instability causing the system to release all the stored energy catastrophically, which ejects the cubes in all directions.

6. Failure modes competition: sliding versus hinging

The previous two sections provided the criteria for the onset of sliding and for the onset of hinging. We now examine and discuss which of the two failure modes may occurs first when the

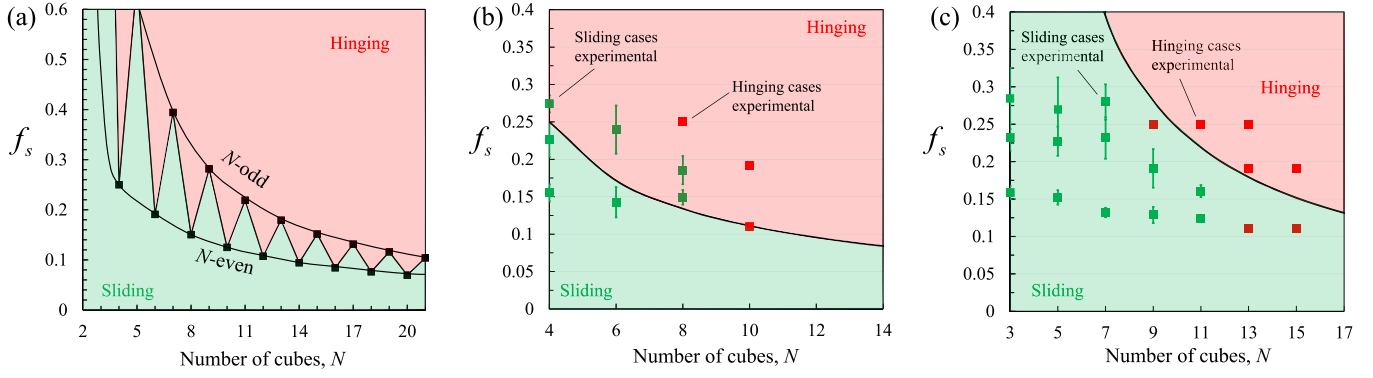


Fig. 11. Deformations maps as function of the friction coefficient f_s and the number of cubes N ; (a) deformation map for odd and even cases; (b-c) comparison of the different combination of (N, f_s) with the actual experimental measurements at the onset of sliding for even cases and odd cases.

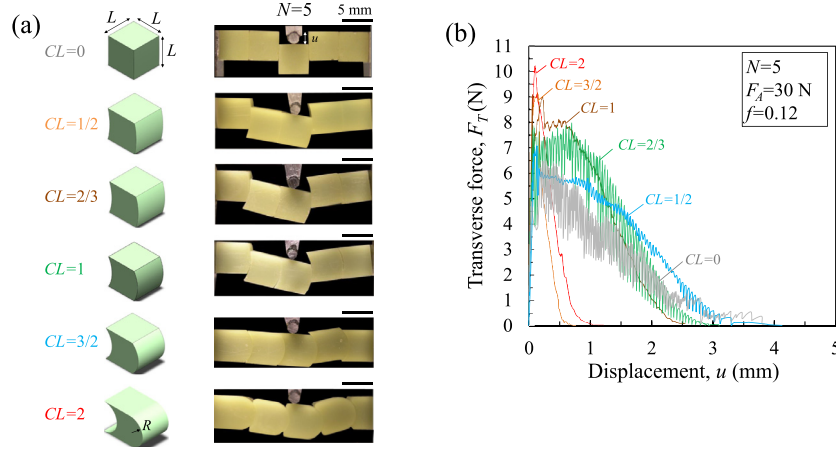


Fig. 12. (a) Enrichment of the blocks with curved contact surfaces with various values of CL (schematics of individual blocks and with corresponding 3D printed samples tested under transverse loading; (b) force-displacement ($F_T - u$) curves for different curvatures: $CL = L/R = 0, 1/2, 2/3, 1, 3/2, 2$.

transverse force F_T is increased. The critical forces for sliding $F_T^{(s)}$ and for hinging $F_T^{(h)}$ only depend on the number of cubes N and on the friction coefficient f_s between the cubes, and therefore one can build a deformation map that depicts the failure mode as function of N and f_s . On this map, the transition between sliding and hinging corresponds to the condition $F_T^{(s)} = F_T^{(h)}$. Using Eqs. (5), (6), (11) and (12), the equations for the transition lines are:

$$4f_s^2(N/4 - 1)^2 - f_s N + 1 = 0 \quad \text{for (even case)} \quad (13a)$$

Which can be solved to give:

$$f_s = \frac{2N - 4\sqrt{2}\sqrt{N-2}}{(N-4)^2} \quad \text{for } N \neq 4 \quad (13b)$$

$$f_s = 0.25 \quad \text{for } N = 4 \quad (13c)$$

$$f_s^2(N/2 - 1)^2 - 2f_s(N/2 - 1) + 1 = 0 \quad \text{for (odd case)} \quad (14)$$

For the cases where N is odd, the transition line equation is solved numerically because Eq. (14) does not have real roots. In these cases the critical sliding force and the critical hinging force cannot strictly be equal $F_T^{(s)} \neq F_T^{(h)}$ because when $F_T = F_T^{(h)}$ the “critical interface” (sliding ones) will lose contact (open) which mean that $|\tau_{xy}/\sigma_{xx}|_{\max} \rightarrow \infty$. For the cases where N is even, the interfaces that lose contact (Fig. 9b) are different than the sliding “critical interfaces” (Fig. 7b). Fig. 11 shows deformation map resulting from these models. As expected sliding prevails for small number of cubes and small friction coefficient, while hinging prevails for large number of cubes and larger friction coefficient. The failure mode transition also depends on whether N is odd or even, but these predictions converge at large N . We emphasize that the

transition between sliding and hinging is independent of the axial compressive force F_A . Interestingly, segmented beams made from cubes with low friction ($f_s < 0.08$) will not hinge (Fig. 11a). We found very good agreement between the theoretical prediction of the failure mode and the experimental observation over the range of f_s and N explored in this work (Figs. 11b, 11c). In the next section we explore another way of manipulating the failure mode by tuning the shape of the cubes.

7. Geometrical enrichments

In terms of structural response, the sliding mode of failure is more beneficial than hinging: Sliding is stable, dissipates energy and only slightly decreases the structural integrity of the beam. In contrast, hinging does not dissipate energy, it is unstable and it weakens the entire system since the forces are transmitted only through a few contact points (A' , B' , C' , P' and Q' on Fig. 9). Segmentation is primarily used to toughen brittle materials, so these contact points which localizes stresses may result in contact fracture. In this section we explore how the geometry of the cubes can be enriched to delay hinging and promote sliding. More specifically, we enrich the geometry of the contacting faces to generate progressive interlocking while at the same time channeling deformations in desired modes. A simple choice that fulfills these requirements is to design contact surfaces with a single curvature of radius R , with $L/2 \leq R \leq +\infty$ (Fig. 12a). The curved faces can be more conveniently described by a non-dimensional curvature $CL=L/R$ with $0 \leq CL \leq 2$. In this study we considered $CL=0$ (flat surface), $CL=1/2$, $CL=2/3$, $CL=1$, $CL=3/2$ and $CL=2$ (maximum curvature, which corresponds to half a circle, Fig. 12a). We tested

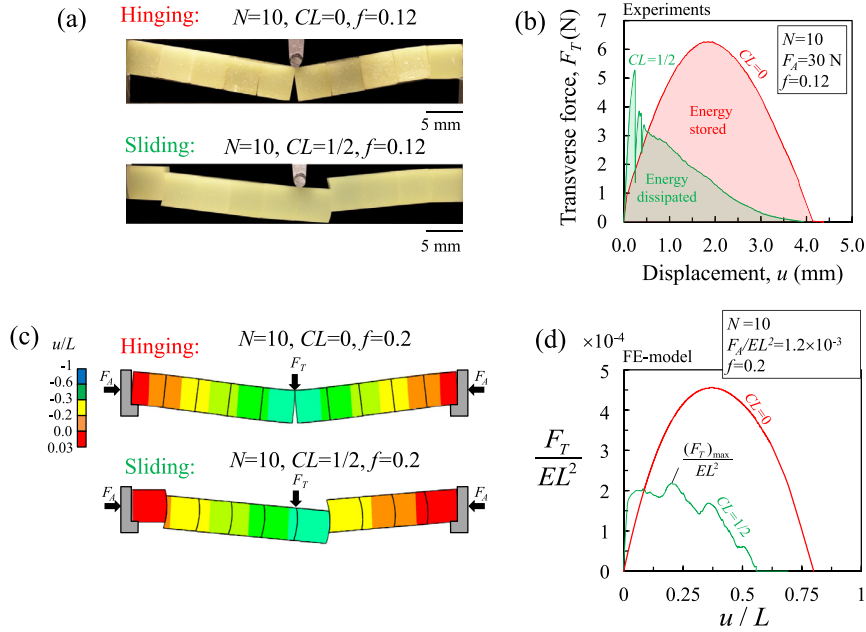


Fig. 13. (a) Example of a contact surface enrichment that prevents hinging in the case $N = 10$; (b) corresponding $F_T - u$ curve for flat case (hinged) and curved case (sliding); (c) deformed architected beam obtained using finite element method (FE) for the cases in (a); (d) $F_T - u$ curves obtained from FE.

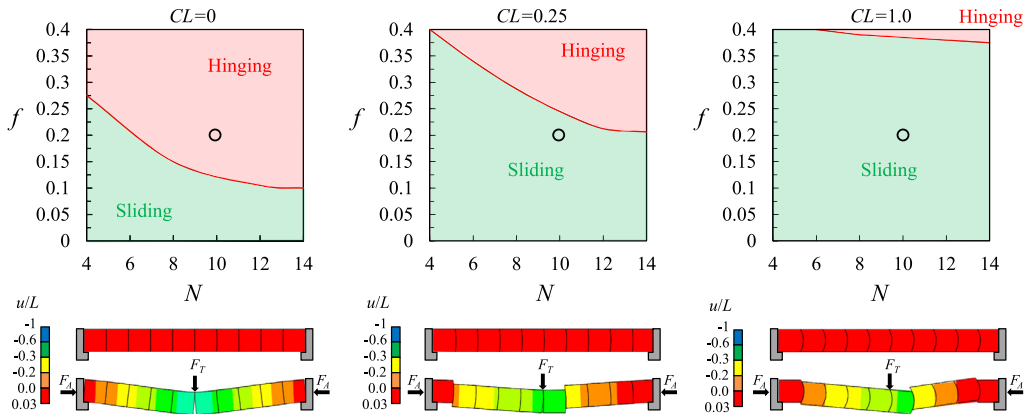


Fig. 14. Deformations maps obtained from FE simulations for different (N, f) . Increasing the curvature CL delays hinging. For each curvature, a deformed beam simulated using FE is shown for $(N = 10, f = 0.2)$.

these different geometries using the same experimental setup described above under a lower axial pre-compression of $F_A = 30$ N to prevent possible yielding at the sharp corners and edges of the blocks. Fig. 12a shows snapshots of the deformation and failure modes for different surface curvatures. $CL = 0$ corresponds to the flat case considered above, where the center block slides. All cases with $CL > 0$ showed a different failure mode where half of the beam rotated collectively in one block. Fig. 12b shows the effect of increasing the curvature on the $F_T - u$ curves. Initially, the curves show a linear elastic rise, showing few drops while rising marking the onset of sliding. During sliding, the volume of material subjected to axial compressive stresses decrease, so that the axial compression F_A decreases. As a result the frictional forces decrease so F_T also decreases progressively. The benefits of curved surfaces become more evident for large number of blocks. Fig. 13 shows the results for $N = 10$, flat and curved interface with $CL = 1/2$. The flat interface led to a hinging type of failure, with a characteristic parabolic shape (Fig. 13b). The energy is stored within the beams, and it is released in a catastrophic failure mode. In contrast, the case $N = 10$ with curved interfaces ($CL = 1/2$) failed by sliding, with frictional energy dissipation and graceful, progressive failure.

The mechanical modeling of arrays of blocks with non-planar contact surfaces is challenging because deformation involves multiple contact points and interlocking of the blocks. Here we capture the transition from hinging to sliding modes using finite element (FE) models (Appendix section A.5, Fig. A.1). The FE model was first validated with experiments (Fig. A.1b) and then used to simulate the sliding and hinging failure modes (Fig. 13b). $F_T - u$ curves from the FE model captured the sliding trend of $CL = 1/2$ and the characteristic parabolic shape of hinging failure mode well (Fig. 13c and d). From the simulated $F_T - u$ curves we obtained the maximum force $(F_T)_{\max}$ (strength) (Fig. 13d). Both experiments and the model show that hinging can improve strength. Hinging becomes advantageous when the system is made from tough blocks (ductile blocks) as in the case of polymer blocks in our experiments. In addition, because hinging depends on the elasticity of the system the strength can be improved by increased E (Khandelwal et al., 2012).

We used the FE model to capture the transition between sliding and hinging as function of number of blocks (focusing on even cases with $N = 4, 6, 8, 10, 12, 14$), as function of friction coefficient ($f = 0$ to 0.4), and as function of surface curvature ($CL = 0, 0.25, 1.0$), for a total of 144 simulations. Fig. 14 shows the resulting

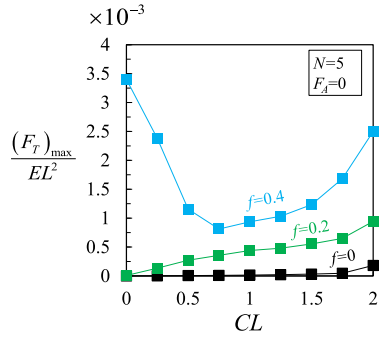


Fig. 15. Strength $(F_T)_{\max}/EL^2$ as function of curvature CL and for different friction coefficients f .

deformation maps for the three different curvatures. Increasing the curvature CL clearly shift the failure transition mode to promote sliding (green region, Fig. 14). The FE models shown for the case $N=10$, $f=0.2$ and for each curvature clearly shows how the curved surface induced sliding and jam the blocks. In addition, the overall strength of the beam depends on the efficacy of the jamming mechanism, which is directly proportional to E . This dependence on E for jamming, is actually similar to hinging which shows that improved strength by storing elastic energy is not exclusive to hinging and that enriched systems that fail by sliding can do so by jamming. However, curved contact surfaces have the added benefit of maintaining contact between blocks which allows sliding that dissipates energy (Fig. 14). Our simulations show that the strength increases with CL (Fig. 15), even with no friction at the interfaces ($f=0$). For high friction, $f=0.4$, and low curvature ($CL=0$ and 0.25), the blocks interlock and show signs of hinging shortly after sliding which explain the high strength values.

8. Summary

We have used experiments and modeling to explore the strength of stability of linear segmented systems made of simple cubes that interact through contact and friction. Using simple tabletop experiments with playing dice, instrumented tests on 3D printed cubes and simple models, we have highlighted the effects of axial pre-compression, number of blocks, friction coefficient and surface morphology on strength and stability. Our main conclusions are as follows:

- 1 Short segmented beams fail by sliding that depends on the friction coefficient f_s . Long and slender segmented beams exhibit nonlinear failure mode where three or four interfaces open into a “hinging” failure mode, with a strength which is independent of f_s .
- 2 The critical transverse force for sliding $F_T^{(s)}$ decreases linearly with increasing N and nonlinearly increases with increasing friction f_s . To properly capture this effect it is necessary to consider the profile of the axial compressive stress as a superposition of the initial axial compressive stresses and of the flexural stresses. A local criterion for the onset of micro-slips at the interface can capture the experimental results.
- 3 The hinging mode of failure only involves elastic deformation no sliding and poor transmission of forces between the blocks. These effects were clearly observed in the beams tested here, and are also present in topologically interlocked panels (Khandelwal et al., 2012; Mirkhalaf et al., 2018b; Siegmund et al., 2016) although their direct observation is more difficult.
- 4 In the context of energy dissipation, toughness and stability, sliding must be promoted over hinging.

- 5 Relatively simple criteria for the onset of sliding or hinging were developed to predict the critical force at sliding $F_T^{(s)}$ and hinging $F_T^{(h)}$. These models capture experimental results quite well. The critical sliding and hinging forces are both proportional to the initial compressive force F_A . The transition between hinging and sliding is strongly dependent on the number of blocks N and on the friction coefficient f_s , but it does not depend on the axial force F_A .
- 6 The morphology of the interfaces between the blocks can be enriched to delay hinging and promote sliding. Here we explored interfaces with simple curvature, which we show maximize contact between the blocks, induce sliding and progressively jam the system. These effects can be captured using finite element models. The curvature of the contact surface is an added design parameter that can be used to optimize its mechanical performance.

These findings can serve as guidelines to design tougher, stronger, reliable and damage tolerant architected beams and plates. Similar to the flat case (cube), the behavior of some architected panels are usually governed by the sliding, tilting, or jamming of the indented block (the block under the load pin). Whereas, for enriched blocks, a group of blocks slide along a designed sliding path. This study also provides insight on the mechanics of spines and helps to understand the interaction of vertebrae during transverse and axial loads. Onset of hinging and sliding may provide a mean to assess the stresses sustained by the intervertebral discs and help determine the effect of flexions (compressive bending) and extensions (tensile bending) (Oxland, 2016). Severe flexural deformation may cause hinging which localizes stresses and increases the likelihood of intervertebral discs herniation, as well as stretching the disc in the tensile side causing disc disruption. Besides, the spine of most reptiles is flexible (Troxell, 1925), subjected to lower stresses (Fronimos et al., 2016), and as this study may suggest is also less prone to hinging than the spines of flatter vertebrae. Finally, this study provides an example of how lateral confinement and friction (analogous to mortar shear strength) may form reliable unreinforced masonry beams. As well as predict the out of plane response of shear walls and the maximum capacity of the mortar between bricks.

Acknowledgments

This work was supported by a Strategic Grant (STPGP 479137-5) from the Natural Sciences and Engineering Research Council of Canada and by a Team Grant (191270) from the Fonds de Recherche du Québec – Nature et Technologies. A.D. was partially supported by a McGill Engineering Doctoral Award.

Appendix

A.1. Load analysis

The system in hand (Fig. 3a) can be modeled as built in continuous beam. Consider the origin to be at the center of the beam where the shear and moment are symmetric about the origin, the moment along the beam can be written as (Ross et al., 1999),

$$\frac{M(x)}{2SF_T} = \frac{1}{8} \left(1 - 2 \frac{|x|}{S} \right) \quad \text{for} \quad -1 \leq \frac{x}{S} \leq 1 \quad (9.1)$$

The magnitude of the bending moment at these locations is $M_{\max} = F_T S/4$ (Fig. 6). These are the locations at which bending stresses are maximum in the beam and where the interfaces between cubes are most prone to opening.

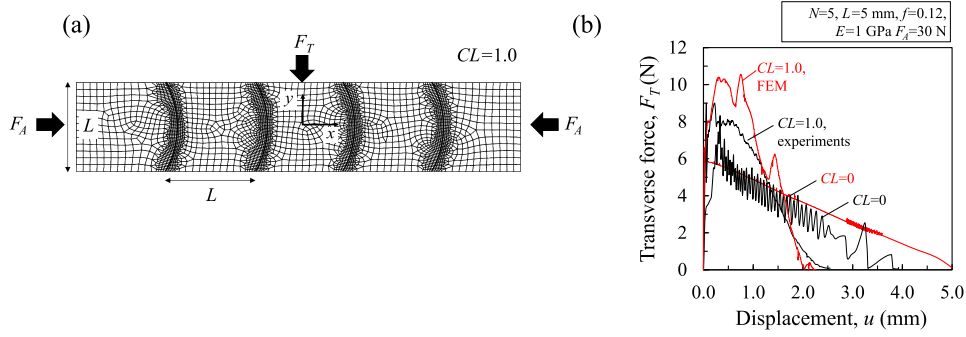


Fig. A.1. Finite element model (FE). (a) meshed beam under axial pre-compression F_A and transverse force F_T ; (b) compare FE results with experiments for validation.

A.2. Stress analysis

The axial stresses in the x -direction σ_{xx} results from the bending stress induced by the moment in the beam $M(x)$ and from the axial compression F_A . Since the system is linear we use superposition to write σ_{xx} and using equilibrium equations to find the shear stress τ_{xy} . Consider the square cross section with moment of inertia ($I=L^4/12$) the stresses are (Timoshenko and Goodier, 1951):

$$\frac{L^2 \sigma_{xx}}{F_A} = 3 \frac{y F_T}{L F_A} \frac{2S}{L} \left(-\frac{1}{2} + \frac{|x|}{S} \right) - 1 \quad \text{for } -1 \leq \frac{x}{S} \leq 1 \quad (9.2a)$$

$$\frac{L^2 \tau_{xy}}{F_A} = -3 \frac{F_T}{F_A} \left[\left(\frac{y}{L} \right)^2 - \frac{1}{4} \right] \quad (9.2b)$$

$L^2 \tau_{xy}/F_A$ follows the well-known parabolic profile, with a maximum value of $(L^2 \tau_{xy}/F_A)_{\max} = 3F_T/4F_A$. Applying only axial compression F_A to the segmented system without any transverse force applied ($F_T = 0$) subjects the interfaces to compressive normal stress only $L^2 \sigma_{xx}/F_A = -1$.

A.3. Pre-sliding behavior

To find the force-displacement curve before the onset of sliding, the stresses σ_{xx} and τ_{xy} can be substituted into the constitutive model (Hooke's law) of the material to find the strain components ε_{xx} , ε_{yy} and γ_{xy} . Integrating the strains and applying boundary conditions we obtain the displacement along y -direction (deflection) (Ross et al., 1999),

$$u_y = \frac{3F_T}{EL^4} (|x| + S)^2 \left(\frac{S}{6} - \frac{|x|}{3} \right) \quad \text{for } \partial u_y / \partial x (x = S, y = 0) = 0 \quad (9.3)$$

the deflection of the beam along the applied load F_T at $x=0$ is given by

$$F_T = \frac{16EL}{N^3} u_y = \frac{16EL}{N^3} u \quad (9.4)$$

deflection at which sliding begins $u = u^{(s)}$ can be expressed as

$$u^{(s)} = \frac{F_T^{(s)} N^3}{16EL} \quad (9.5)$$

A.4. Post sliding behavior

The system lateral axial force relaxes when sliding start, which reduces the initial lateral compressive force F_A . The whole system losses compressive traction at the trailing edge of the sliding cubes while part of interface that are still in contact with the adjacent cube retain compressive stress. Therefore, the portion of material held in between the cubes is subjected to decreasing compressive

stress of $\sigma = F_A/L(L-u)$. Using the constitutive relation (Hooke's law), the strain is found to be $\varepsilon = F_A/L(L-u) = 2\Delta/NL$, where Δ is the axial displacement due to axial compression. Realizing that the cubes resemble spring in series, the equivalent stiffness of the system can be described by: $K_{eq} = \frac{E(L-u)}{N}$, using the equivalent spring equation: $F_A = K_{eq} 2\Delta$ we get:

$$F_A(u) = \frac{F_A(L-u)}{L} \quad \text{for } u^{(s)} \leq u \leq L \quad (9.6)$$

Setting $u=0$ in Eq. (9.6) returns the "initial" axial compressive force (precompression) F_A . After the onset of sliding, Coulomb's sliding criterion ($F_{interface}^{(s)} = f_d F_A$) is used to capture the onset of incremental sliding at varying compressive force as function of displacement, $F_A(u)$. Accordingly, the force-displacement curve is described by $F_T = 2f_d F_A$ giving:

$$\frac{F_T}{F_A} = f_d \left(1 - \frac{u}{L} \right) \quad \text{for } u^{(s)} \leq u \leq L \quad (9.7)$$

where f_d is the dynamic friction coefficient.

A.5. Finite element model of curved interfaces

To test the effect of interface enrichment, we modeled the architected beam using finite element (FE) (Fig. A.1). The blocks are modeled based on continuum with linear elastic behavior with Young's modulus, E and poisson's ratio $\nu=0.2$. The blocks are meshed using 8 nodes quadratic plane stress elements (PLANE183 (ANSYS, 2013b)). The blocks are separated by contact elements (CONTA 172, (ANSYS, 2013a)), that consider contact deformation and contact friction. The beam rests on rigid supports modeled as rigid contact elements (TARGE 169, (ANSYS, 2013a)), the beam is subjected to axial pre-compression F_A applied at both ends ($x=\pm L/2, y=0$) and to a transverse force F_T applied at $x=0, y=L/2$. The FE model will be used to obtain F_T-u curve for different CL, f, N . Mesh is refined until results are mesh independent, in addition it is compared with experiments for validation (Fig. A.1b).

Reference

- Ahueidda, D.W., Abu Al-Rub, R.K., Dalaq, A.S., Lee, D.-W., Khan, K.A., Jasiuk, I., 2016. Effective conductivities and elastic moduli of novel foams with triply periodic minimal surfaces. *Mech. Mater.* 95, 102–115.
- Alben, S., Madden, P.G., Lauder, G.V., 2007. The mechanics of active fin-shape control in ray-finned fishes. *J. R. Soc. Interface* 4, 243–256.
- ANSYS, 2013a. ANSYS Mechanical APDL Contact Technology Guide. ANSYS Release 15.0.
- ANSYS, 2013b. ANSYS Mechanical APDL Modeling and Meshing Guide, November 2013 ed. ANSYS Release 15.0.
- Ashby, M.F., 2005. Hybrids to fill holes in material property space. *Philos. Mag.* 85, 3235–3257.
- Ashby, M.F., 2006. The properties of foams and lattices. *Philos. Trans. R. Soc. A* 364, 15–30.
- Ashby, M.F., Evans, T., Fleck, N.A., Hutchinson, J.W., Wadley, H.N.G., Gibson, L.J., 2000. *Metal Foams: A Design Guide*. Elsevier.

- ASTM, 1894. Standard Test Method for Static and Kinetic Coefficients of Friction of Plastic Film and Sheeting (D1894). ASTM.
- Barthelat, F., 2014. Designing nacre-like materials for simultaneous stiffness, strength and toughness: optimum materials, composition, microstructure and size. *J. Mech. Phys. Solids* 73, 22–37.
- Barthelat, F., 2015. Architected materials in engineering and biology: fabrication, structure, mechanics and performance. *Int. Mater. Rev.* 60, 413–430.
- Barthelat, F., Yin, Z., Buehler, M.J., 2016a. Structure and mechanics of interfaces in biological materials. *Nat. Rev. Mater.* 1.
- Barthelat, F., Yin, Z., Buehler, M.J., 2016b. Structure and mechanics of interfaces in biological materials. *Nat. Rev. Mater.* 1, 16007.
- Begley, M.R., Phillips, N.R., Compton, B.G., Wilbrink, D.V., Ritchie, R.O., Utz, M., 2012. Micromechanical models to guide the development of synthetic ‘brick and mortar’ composites. *J. Mech. Phys. Solids* 60, 1545–1560.
- Ben-David, O., Cohen, G., Fineberg, J., 2010. The dynamics of the onset of frictional slip. *Science* 330, 211–214.
- Ben-David, O., Fineberg, J., 2011. Static friction coefficient is not a material constant. *Phys. Rev. Lett.* 106, 254301.
- Berman, A.D., Ducker, W.A., Israelachvili, J.N., 1996. Origin and characterization of different stick–slip friction mechanisms. *Langmuir* 12, 4559–4563.
- Chen, L., Ballarini, R., Kahn, H., Heuer, A.H., 2007. Bioinspired micro-composite structure. *J. Mater. Res.* 22, 124–131.
- Chintapalli, R.K., Mirkhalaf, M., Dastjerdi, A.K., Barthelat, F., 2014. Fabrication, testing and modeling of a new flexible armor inspired from natural fish scales and osteoderms. *Bioinspir. Biomim.* 9, 036005.
- Dalaq, A.S., Abueidda, D.W., Abu Al-Rub, R.K., 2016. Mechanical properties of 3D printed interpenetrating phase composites with novel architected 3D solid-sheet reinforcements. *Compos. Part A* 84, 266–280.
- Dawood, A., Marti, B.M., Sauret-Jackson, V., Darwood, A., 2015. 3D printing in dentistry. *Br. Dent. J.* 219, 521–529.
- Dimas, L.S., Bratzel, G.H., Eylon, I., Buehler, M.J., 2013. Tough composites inspired by mineralized natural materials: computation, 3D printing, and testing. *Adv. Funct. Mater.* 23, 4629–4638.
- Dugué, M., Fivel, M., Bréchet, Y., Dendievel, R., 2013. Indentation of interlocked assemblies: 3D discrete simulations and experiments. *Comput. Mater. Sci.* 79, 591–598.
- Dunn, I.F., Proctor, M.R., Day, A.L., 2006. Lumbar spine injuries in athletes. *Neurosurg. Focus* 21, E4.
- Dyskin, A.V., Estrin, Y., Kanel-Belov, A.J., Pasternak, E., 2001. Toughening by fragmentation—how topology helps. *Adv. Eng. Mater.* 3, 885–888.
- EnvisionTEC | Desktop, 2019. Professional and Industrial 3D Printers. EnvisionTEC.
- Escobar de Obaldia, E., Herrera, S., Grunenfelder, L.K., Kisailus, D., Zavattieri, P., 2016. Competing mechanisms in the wear resistance behavior of biomineralized rod-like microstructures. *J. Mech. Phys. Solids* 96, 511–534.
- Fratzl, P., Kolednik, O., Fischer, F.D., Dean, M.N., 2016. The mechanics of tessellations - bioinspired strategies for fracture resistance. *Chem. Soc. Rev.* 45, 252–267.
- Fronimos, J.A., Wilson, J.A., Baumiller, T.K., 2016. Polarity of concavo-convex intervertebral joints in the necks and tails of sauropod dinosaurs. *Paleobiology* 42, 624–642.
- Gibson, L.J., Ashby Michael, F., Schajer, G.S., Robertson, C.I., 1982. The mechanics of two-dimensional cellular materials. *Proc. R. Soc. Lond. A. Math. Phys. Sci.* 382, 25–42.
- Johnson, K.L., 1987. *Contact Mechanics*. Cambridge University Press.
- Kammer, D.S., Radiguet, M., Ampuero, J.-P., Molinari, J.-F., 2015. Linear elastic fracture mechanics predicts the propagation distance of frictional slip. *Tribol. Lett.* 57, 23.
- Khandelwal, S., Siegmund, T., Cipra, R.J., Bolton, J.S., 2012. Transverse loading of cellular topologically interlocked materials. *Int. J. Solids Struct.* 49, 2394–2403.
- Martini, R., Balit, Y., Barthelat, F., 2017. A comparative study of bio-inspired protective scales using 3D printing and mechanical testing. *Acta Biomater.* 55, 360–372.
- Martini, R., Barthelat, F., 2016. Stretch-and-release fabrication, testing and optimization of a flexible ceramic armor inspired from fish scales. *Bioinspir. Biomim.* 11, 066001.
- Menezes, P., Ingole, S.P., Nosonovsky, M., Kailas, S.V., Lovell, M.R., 2013. *Tribology for Scientists and Engineers: From Basics to Advanced Concepts*. Springer-Verlag, New York.
- Ming-Yuan, H., Hutchinson, J.W., 1989. Crack deflection at an interface between dissimilar elastic materials. *Int. J. Solids Struct.* 25, 1053–1067.
- Mirkhalaf, M., Dastjerdi, A.K., Barthelat, F., 2014. Overcoming the brittleness of glass through bio-inspiration and micro-architecture. *Nat. Commun.* 5.
- Mirkhalaf, M., Sunesara, A., Ashrafi, B., Barthelat, F., 2018a. Toughness by segmentation: fabrication, testing and micromechanics of architected ceramic panels for impact applications. *Int. J. Solids Struct.* 158, 52–65.
- Mirkhalaf, M., Tanguay, J., Barthelat, F., 2016. Carving 3D architectures within glass: exploring new strategies to transform the mechanics and performance of materials. *Extrem. Mech. Lett.* 7, 104–113.
- Mirkhalaf, M., Zhou, T., Barthelat, F., 2018b. Simultaneous improvements of strength and toughness in topologically interlocked ceramics. *Proc. Natl Acad. Sci.* 115, 9128–9133.
- Molnar, J.L., Pierce, S.E., Bhullar, B.-A.S., Turner, A.H., Hutchinson, J.R., 2015. Morphological and functional changes in the vertebral column with increasing aquatic adaptation in crocodylomorphs. *Open Sci.* 2, 150439.
- Naleway, S.E., Porter, M.M., McKittrick, J., Meyers, M.A., 2015. Structural design elements in biological materials: application to bioinspiration. *Adv. Mater.* 27, 5455–5476.
- Oxland, T.R., 2016. Fundamental biomechanics of the spine—What we have learned in the past 25 years and future directions. *J. Biomech.* 49, 817–832.
- Porter, M.E., Ewoldt, R.H., Long, J.H., 2016. Automatic control: the vertebral column of dogfish sharks behaves as a continuously variable transmission with smoothly shifting functions. *J. Exp. Biol.* 219, 2908–2919.
- Ritchie, R.O., 2011. The conflicts between strength and toughness. *Nat. Mater.* 10, 817–822.
- Robert, L.M., 1960. A comprehensive classification of shape-variants of vertebrae. *Turtox News* 38.
- Ross, C.T.F., Case, T.I.J., Chilver, A., 1999. *Strength of Materials and Structures*. Elsevier.
- Rubinstein, S.M., Cohen, G., Fineberg, J., 2004. Detachment fronts and the onset of dynamic friction. *Nature* 430, 1005–1009.
- Schaefer, J.T., Summers, A.P., 2005. Batoid wing skeletal structure: novel morphologies, mechanical implications, and phylogenetic patterns. *J. Morphol.* 264, 298–313.
- Scheibert, J., Dysthe, D.K., 2010. Role of friction-induced torque in stick-slip motion. *EPL* 92, 54001.
- Siegmund, T., Barthelat, F., Cipra, R., Habtour, E., Riddick, J., 2016. Manufacture and mechanics of topologically interlocked material assemblies. *Appl. Mech. Rev.* 68, 040803-040803.
- Stuart, A.R., 2016. Additive manufacturing of biologically-inspired materials. *Chem. Soc. Rev.* 45, 359–376.
- Szewciw, L., Zhu, D., Barthelat, F., 2017. The nonlinear flexural response of a whole teleost fish: contribution of scales and skin. *J. Mech. Behav. Biomed. Mater.* 76, 97–103.
- by Timoshenko, S., Goodier, J.N., 1951. In: Timoshenko, S., Goodier, J.N. (Eds.), *Theory of Elasticity*, Second ed. McGraw-Hill Book Company. by...
- Troxell, E.L., 1925. Mechanics of crocodile vertebrae. *GSA Bull.* 36, 605–614.
- Tumbleston, J.R., Shirvanyants, D., Ermoshkin, N., Januszewicz, R., Johnson, A.R., Kelly, D., Chen, K., Pinschmidt, R., Rolland, J.P., Ermoshkin, A., Samulski, E.T., DeSimone, J.M., 2015. Continuous liquid interface production of 3D objects. *Science* 347, 1349–1352.
- Wadley, H.N.G., O’Masta, M.R., Dharmasena, K.P., Compton, B.G., Gamble, E.A., Zok, F.W., 2013. Effect of core topology on projectile penetration in hybrid aluminum/alumina sandwich structures. *Int. J. Impact Eng.* 62, 99–113.
- Wegst, U.G.K., Bai, H., Saiz, E., Tomsia, A.P., Ritchie, R.O., 2015. Bioinspired structural materials. *Nat. Mater.* 14, 23–36.
- Yang, W., Chen, I.H., Gludovatz, B., Zimmermann, E.A., Ritchie, R.O., Meyers, M.A., 2013. Natural flexible dermal armor. *Adv. Mater.* 25, 31–48.
- Zhu, H.P., Zhou, Z.Y., Yang, R.Y., Yu, A.B., 2008. Discrete particle simulation of particulate systems: a review of major applications and findings. *Chem. Eng. Sci.* 63, 5728–5770.